chemosensors

MDPI

Article

Nanorods Assembled Hierarchical Bi_2S_3 for Highly Sensitive Detection of Trace NO_2 at Room Temperature

Yongchao Yang [1,2], Chengli Liu [2], You Wang [1] and Juanyuan Hao [1,*]

[1] School of Materials Science and Engineering, Harbin Institute of Technology, Harbin 150001, China; yangyongchao1987@163.com (Y.Y.); y-wang@hit.edu.cn (Y.W.)
[2] The 49th Research Institute of China Electronics Technology Group Corporation, Harbin 150028, China; 13613669698@139.com
* Correspondence: jyhao@hit.edu.cn; Tel.: +86-0451-86492590

Abstract: The bismuth sulfide nanostructure has become a promising gas sensing material thanks to its exceptional intrinsic properties. However, pristine Bi_2S_3 as a room-temperature sensing material cannot achieve the highly sensitive detection of ppb-level NO_2 gas. Herein, 1D nanorods with self-assembled hierarchical Bi_2S_3 nanostructures were obtained via a simple hydrothermal process. The as-prepared hierarchical Bi_2S_3 nanostructures exhibited outstanding NO_2 sensing behaviors, such as a high response value (R_g/R_a = 5.8) and a short response/recovery time (τ_{90} = 28/116 s) upon exposure to 1 ppm NO_2. The limit of detection of hierarchical Bi_2S_3 was down to 50 ppb. Meanwhile, the sensor exhibited excellent selectivity and humidity tolerance. The improved NO_2 sensing properties were associated with the self-assembled hierarchical nanostructures, which provided a rich sensing active surface and accelerated the diffusion and adsorption/desorption processes between NO_2 molecules and Bi_2S_3 materials. Additionally, the sensing response of hierarchical Bi_2S_3 nanostructures is much higher at 100% N_2 atmosphere, which is different from the chemisorption oxygen model.

Keywords: hierarchical Bi_2S_3; NO_2 detection; high sensitivity; room temperature

check for updates

Citation: Yang, Y.; Liu, C.; Wang, Y.; Hao, J. Nanorods Assembled Hierarchical Bi_2S_3 for Highly Sensitive Detection of Trace NO_2 at Room Temperature. *Chemosensors* **2024**, *12*, 8. https://doi.org/10.3390/chemosensors12010008

Academic Editor: Takahiro Arakawa

Received: 4 December 2023
Revised: 31 December 2023
Accepted: 3 January 2024
Published: 4 January 2024

1. Introduction

Nitrogen dioxide (NO_2), as a typically hazardous gas released from the burning of fossil fuels, can trigger serious environmental and health problems [1,2]. As reported, continuous exposure to trace NO_2 gas may cause respiratory diseases such as chronic bronchitis, asthma, and emphysema [3–9]. The U.S. Environmental Protection Agency sets 53 ppb NO_2 as the ambient exposure concentration standard. Meanwhile, ppb-level NO_2 gas detection can contribute to auxiliary diagnoses of humans' physical health, such as lung disease and gastrointestinal disorder symptoms [10–12]. Chemiresistive gas sensors based on metal oxides have shown superb NO_2 sensing properties, such as high sensitivity and a short response time [13]. However, such NO_2 sensors generally need a high operating temperature to obtain high sensitivity, fast response/recovery speed, and a low limit of detection (LOD). The high working temperature brings about extra power consumption and triggers safety problems, which seriously restrict their potential application in medical treatment and environmental monitoring [14–16]. With the rapid development of the emerging 5G network and the Internet of Things, it is very important to research new room-temperature (RT) sensing materials for highly sensitive trace NO_2 detection.

The layer metal chalcogenides as sensing nanomaterials were extensively researched in the gas sensor field for recognizing low-concentration NO_2 molecules at RT due to their unique physicochemical properties. Among them, Bi_2S_3 nanostructured materials have a tunable bandgap of 1.3–1.7 eV [17–20] and high carrier mobility of about 10^3 cm^2 V^{-1} s^{-1} [21,22], which can facilitate the electron transfer process between Bi_2S_3-based sensing materials and target gas molecules at RT. Bi_2S_3-based gas sensors have been used for various gas detections, such as H_2 [23], NH_3 [24], H_2S [25], etc. In recent years, Bi_2S_3

nanostructures as RT NO_2 sensing materials have gained widespread attention due to their excellent affinity for NO_2 molecules [26]. For example, Liu et al. reported that synthesized Bi_2S_3 nanobelts showed superior RT NO_2 sensing performance, such as a short response time and superb selectivity [21]. Yang et al. reported that the Au/Bi_2S_3 heterojunction nanosheets exhibited rapid sensing response and outstanding selectivity toward NO_2 gas at RT, which was associated with the increasing active sites and accelerated electron transfer arising from sulfur vacancies [27]. Zhang et al. constructed a CuS/Bi_2S_3 nanosheet sensor, which exhibited excellent NO_2 sensing response at RT due to a mass of sensing active sites and quantum size effect [28]. Unfortunately, Bi_2S_3-based gas sensors display some poor RT NO_2 sensing properties, such as a long recovery time and a high LOD, which severely impede their spread and applications [21,29].

As we know, the morphology and structure characteristics of gas sensing materials play a key role in improving sensing behaviors because the sensing properties depend on the diffusion and adsorption/desorption processes between the sensing materials and the target gas. Low-dimension nanostructures (nanobelts, nanorods, and nanosheets) easily stack and aggregate together, which would reduce the active surface to adsorb gas molecules and obstruct gas diffusion and adsorption/desorption processes, weakening the sensing materials intrinsic sensing properties. Low-dimensional nanostructures can effectively avoid restacking together and obviously increase active surface via the constructed hierarchical nanostructures method, which can provide rich sensing active sites and promote detection of gas diffusion and adsorption/desorption on the surface of nanomaterials. For example, Liu et al. prepared hierarchical SnS_2 nanoflowers, which showed excellent low NO_2 LOD due to the mass of the available surface-active sites [30]. Wang et al. synthesized the nanoplate-assembled $SnSe_2$ nanoflowers, which exhibited a highly sensitive response to ppb-level NO_2 at RT [31]. Zhang et al. reported that hierarchical MoS_2 nanospheres improved the sensing behaviors toward NO_2 gas due to the open 3D nanostructure and abundant reaction active sites [32]. The hierarchical nanostructured Bi_2S_3 (flower-like, urchin-like, sheaf-like, etc.) have been successfully prepared through various means in order to elevate their functional properties [24,33–36]. For example, Fu prepared a 3D Bi_2S_3 nanowire network, which showed excellent sensing properties for NH_3 at RT due to its large surface area [24]. Therefore, constructed hierarchical Bi_2S_3 nanomaterials are an effective approach to enhance their NO_2-sensitive properties, which may provide a new route for optimizing nanostructures to enhance the sensing behaviors of low-dimensional nanomaterials.

Herein, 1D nanorods with self-assembled Bi_2S_3 hierarchical nanostructures were prepared using a facile hydrothermal procedure. As-prepared Bi_2S_3 nanomaterials showed hierarchical morphology, which was conducive to a mass of NO_2 molecules rapidly diffused inward and adsorbed on the surface of the hierarchical Bi_2S_3 nanostructure materials to enhance their gas sensing performance. The NO_2 sensors based on 1D nanorods and self-assembled Bi_2S_3 sensing materials showed high sensitivity, rapid response/recovery speed, and a low LOD for NO_2 at RT. These findings demonstrated that the constructed hierarchical Bi_2S_3 nanostructures serve as promising candidates for hypersensitive NO_2 detection devices.

2. Materials and Methods

2.1. Synthesis of Hierarchical Bi_2S_3 Nanomaterials

Hierarchical Bi_2S_3 nanostructures assembled from 1D nanorods were obtained via facile hydrothermal means inspired by the previous studies [37,38]. Typically, 303 mg of $Bi(NO_3)_3{\cdot}5H_2O$ powder was dispersed in 30 mL of deionized water with vigorous mixing for 30 min, forming a milky suspension. Then, 476 mg of CH_4N_2S powder was added to the above suspension, followed by continuous mixing for 60 min to form a yellow reaction solution. The above mixture was sealed in a 50 mL hydrothermal reactor. Subsequently, the above solution was heated to 140 °C and kept for 12 h. After naturally cooling down to ambient temperature, the black powder was collected via centrifugation and washed with

ethanol and deionized water 3 times. Finally, the obtained product was dried at 60 °C for 12 h.

To study the formation mechanism of the 1D nanorods self-assembled in Bi_2S_3 hierarchical structures, a series of samples were prepared by adjusting the hydrothermal reaction time from 0 h to 24 h. The corresponding samples were named BS-*X*, where *X* stands for the hydrothermal reaction time in an hour.

2.2. Material Characterizations

The crystal structure information of the as-prepared materials was acquired using a Bruker D8 Advance X-ray diffractometer (Bruker Technology Co., LTD, Saarbrucken, Germany). The scanning electron microscopy images of the as-prepared powder were acquired with a Zeiss Sigma 300 (Carl Zeiss AG, Oberkochen, Germany). The high-resolution transmission electron microscopy was carried out on a FEI Talos F200S (FEI Company, Hillsboro, OR, USA). The information on the surface chemical states of the obtained product was studied via X-ray photoelectron spectroscopy (Thermo Scientific K-Alpha spectrometer, Thermo Fisher Scientific, Waltham, MA, USA). The Brunauer–Emmett–Teller (BET)-specific surface area was measured with a Micromeritics ASAP 2460 apparatus (Micromeritics Instruments Corporation, Norcross, GA, USA).

2.3. Gas Sensing Measurements

First, the mixture containing the as-prepared Bi_2S_3 powder (10 mg) and ethanol (1 mL) was prepared. Then, the 20 μL above mixture was coated on an Al_2O_3 substrate with Ag-Pd interdigitated electrodes to form a sensing film. Finally, the thin-film gas sensor was dried in a vacuum chamber at 60 °C for 3 h. The detailed parameters of the sensing device are shown in Figure S1.

Gas sensing properties were obtained using a homemade gas sensor test system, as in our previous work [39]. The dynamic gas sensor test system was employed to investigate the sensing mechanism (Figure S2). As-prepared sensors based on different sensing materials were aged for 24 h under a 5 V voltage at RT before the sensing test. The relative humidity (RH) of the testing chamber was controlled with the humidity generator. The real-time resistance information of the sensors was recorded using the electrochemical workstation. The known concentration of detection gas rapidly flowed through the testing chamber. The sensing response value (S) was calculated using the equation: $S = R_a/R_g$ (when $R_a > R_g$) and R_g/R_a (when $R_a < R_g$), where R_g and R_a were the RT resistance values recorded in detection gas and clean air, respectively. Herein, the response and recovery times (τ_{90}) were defined as the time to reach 90% of the total resistance variation during gas-in and gas-out, respectively.

3. Results

3.1. Morphology and Structure

The hierarchical Bi_2S_3 nanostructures are obtained through a one-step hydrothermal process, and their structures are highly dependent on synthesized time (as shown in Figure 1a). The as-prepared hydrolysis product shows 1D rod-like structures, as shown in the SEM image (Figure 1b). According to the calculated method of standard deviation by measuring 20 rod-like structures, the diameter of rod-like structures is about 1.2 μm. Subsequently, many nanowire-assembled microsphere structures appear after a hydrothermal reaction for 1 h (Figure 1c). With increasing hydrothermal reaction for 12 h, the as-prepared sample shows 1D nanorods of self-assembled hierarchical Bi_2S_3 structures with a diameter of about 4.0 μm (Figure 1d). The length of self-assembled nanorods is approximately 2.0 μm, with a diameter of about 150 nm. The TEM and HRTEM images further show the hierarchical nanostructures of the synthesized Bi_2S_3 sample (Figure 1e,f). These hierarchical Bi_2S_3 nanostructures can efficaciously prevent the 1D nanorods from restacking together, which may dramatically add exposure sensing sites and facilitate the diffusion and adsorption/desorption processes of gas molecules. The 1D nanorods assembled into

hierarchical nanostructures would show superior sensing behaviors than those of only 1D nanorods [40,41]. The EDS mapping confirms the uniform distribution of Bi and S elementals along the full hierarchical Bi_2S_3 (Figure S3). The EDS spectrum of the as-prepared Bi_2S_3 sample further demonstrates the sample consists of Bi and S without other elementals, and the atomic ratio of Bi to S of the sample almost meets the stoichiometry ratio.

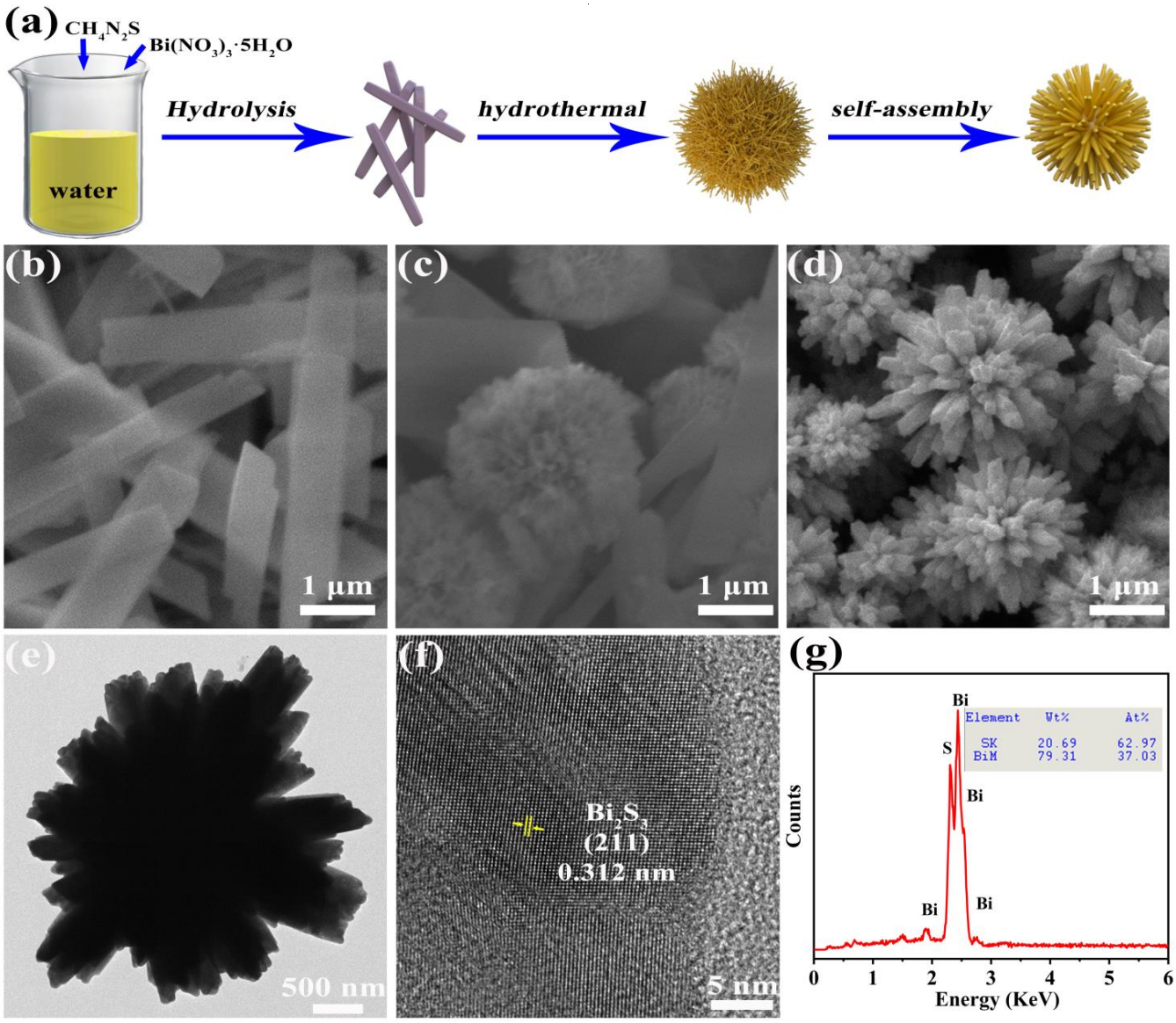

Figure 1. (**a**) Schematic illustration of the formation process of hierarchical Bi_2S_3 nanomaterials. SEM images of the hydrolysis product (**b**), the as-prepared sample with a 1 h hydrothermal reaction time (**c**), and the sample with a 12 h reaction (**d**); TEM (**e**) and (**f**) HRTEM images; and the EDS spectrum of the BS-12h sample (**g**).

In order to obtain the formation mechanism of the hierarchical Bi_2S_3 nanostructures, serious samples with different reaction times were prepared and analyzed, combined with XRD patterns and SEM images. Firstly, $Bi(NO_3)_3{\cdot}5H_2O$ powder was dispersed in deionized water and generated hydrolysis, which resulted in the formation of a milky solution. The obtained white hydrolysate shows 1D nanorod structures (Figure 1b). As shown in Figure 2a, the appearing XRD spectrum peaks of the hydrolysis product conform to the bismuth oxide hydroxide nitrate hydrate (JCPDF no. 70-1226). Subsequently, with CH_4N_2S added to the homogeneous solution, the color of the above solution became yellow due to $[Bi(CH_4N_2S)n]^{3+}$ chelates from the strong reaction between Bi^{3+} and CH_4N_2S [34,42].

Secondly, the CH_4N_2S of the reaction mixture could decompose to generate H_2S under 140 °C, which would react with the Bi^{3+} to form Bi_2S_3 nanocrystals. At the early stage of the hydrothermal reaction for 1 h, the Bi_2S_3 nanostructures were confirmed with the XRD pattern. With increasing the reaction time from 2 h to 8 h, the microspheres gradually transfer to 1D nanorods assembled into hierarchical nanostructures (Figure S4a–d) [43]. The microsphere structures of the BS-12h sample almost disappear, and the assembled 1D nanorods of hierarchical nanostructures become sturdy and short, with the reaction process lasting 24 h (Figure S4e–f). The diffraction peaks of as-prepared Bi_2S_3 samples at 2θ = 15.8°, 17.6°, 22.4°, 24.9°, 28.6°, 31.8°, 39.0°, 46.5°, and 52.6° match well with (020), (120), (220), (130), (211), (221), (041), (431), and (351) planes of orthorhombic Bi_2S_3 (JCPDF no. 17-0320). The intensity of diffraction peaks in the prepared sample shows inconspicuous variation after hydrothermal reaction time over 4 h. The sharp diffraction peaks without any other impurity phase confirm the high purity of the prepared Bi_2S_3.

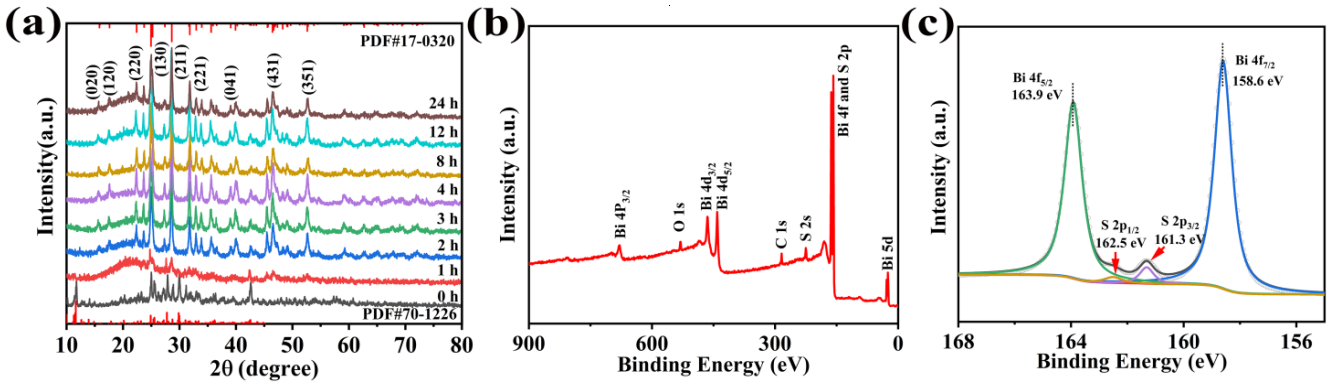

Figure 2. (**a**) XRD patterns of prepared samples with different reaction times. (**b**) XPS survey; (**c**) Bi_{4f} and S_{2p} core level spectrum of the BS-12h sample.

The information on the surface chemical states of the as-prepared hierarchical Bi_2S_3 sample was obtained via XPS. The XPS survey spectrum of the BS-12h sample is shown in Figure 2b. The highly pure Bi_2S_3 is further confirmed. The high-resolution XPS spectra of the Bi 4f and the S 2p are shown in Figure 2c. The Bi 4f core level spectrum of the hierarchical Bi_2S_3 shows the Bi $4f_{7/2}$ and Bi $4f_{5/2}$ strong peaks at 158.6 and 163.9 eV, respectively [44,45]. The peaks located at 161.3 and 162.5 eV can be assigned to S $2p_{3/2}$ and S $2p_{1/2}$, respectively, confirming the existence of S^{2-} [44,45]. All the above results demonstrate that the hierarchical Bi_2S_3 was prepared successfully.

3.2. Characterization of Gas Sensing Performance

In order to demonstrate the internal linkage between morphologies and structures with sensing characteristics, the RT sensing properties of the as-prepared BS-8h, BS-12h, and BS-24h samples were measured using a dynamic gas sensor analysis system. The RT dynamic sensing response curves of the above sensors (BS-8h, BS-12h, and BS-24h) for low concentration NO_2 ranging from 0.1 to 1.0 ppm are shown in Figure 3a. All sensors show typical n-type semiconductor sensing behaviors, and the sensing response resistance gradually increases with increasing exposure to NO_2 concentration. Figure 3b displays the linear relationship of all prepared sensors between sensitivity and NO_2 concentration. The BS-12h sensor shows high sensitivity and a good linear relationship to trace NO_2 gas at RT. The RT response/recovery curves of the BS-8h, BS-12h, and BS-24h sensors upon exposure to 1 ppm NO_2 are shown in Figure S5. The sensors based on the hierarchical Bi_2S_3 display superb response/recovery properties. The response and recovery time of the sensor based on the BS-12h sample toward 1 ppm NO_2 were 28 and 116 s, respectively. These results show that the 1D nanorod self-assembled Bi_2S_3 structures have superior RT NO_2 sensing responses, which could be ascribed to the special hierarchical nanostructures. According to

the test results, the BS-12h sample was chosen as a promising sensing material for sensors after deeply appraising its NO_2 sensing properties.

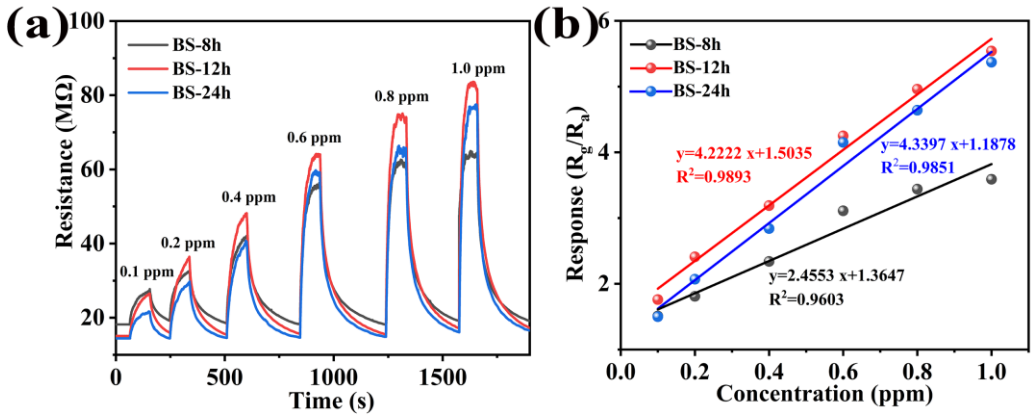

Figure 3. RT NO_2 sensing performance of BS-8h, BS-12h, and BS-24h samples: (**a**) dynamic sensing response curves and (**b**) the corresponding linear relationship between sensitivity and NO_2 concentration ranging from 0.1 to 1.0 ppm.

The RT dynamic response curve of the BS-12h sensor with varied NO_2 concentrations is shown in Figure 4a. The recorded real-time response resistance value exhibits an increasing trend when the concentration of NO_2 increases from 50 ppb to 10 ppm. The main reason may be associated with more NO_2 molecules trapped on the surface of hierarchical nanomaterials and obtaining more electrons from the surface of the Bi_2S_3 nanostructure. Meanwhile, the BS-12h sensor displays fast response speed and full-recovery sensing properties, which could be ascribed to the hierarchical nanostructures of the Bi_2S_3 materials. These results confirm the BS-12h sensor can effectively realize low-concentration NO_2 detection from 50 ppb to 10 ppm at RT. The sensor based on hierarchical Bi_2S_3 nanostructures displays two sectional linear relations between sensitivity and NO_2 concentration from 0.05 to 2 ppm and 2 to 10 ppm (Figure 4b). These phenomena were associated with decreasing carrier mobility due to the scattering effects of adsorbed gas molecules on the surface of sensing materials [46,47].

The humidity tolerance ability of the BS-12h sensor was investigated considering the practical application of the gas sensor. The response resistance curves of the Bi_2S_3-based sensors to 1 ppm NO_2 under different relative humidity levels from 15% to 85% are shown in Figure 4c. The sensor based on hierarchical Bi_2S_3 nanostructures displays excellent response/recovery properties under different relative humidity conditions. The RT resistance value of the BS-12h sensor sustainably declines as the relative humidity gradually increases (Figure 4d), which may be attributed to the increased electron density of Bi_2S_3 sensing materials. As ambient relative humidity increases, abundant H_2O molecules adsorbed on the surface of the Bi_2S_3 nanostructures act as electron donors [48–50]. The electrons will transfer from H_2O molecules to the surface of Bi_2S_3 nanostructures, which leads to increased conductivity in the Bi_2S_3 sensor. The sensitivity of the BS-12h sensor exhibits a downward trend from 5.8 to 4.1 as ambient humidity increases from 15% RH to 85% RH. The calculated sensitivity deviation of the BS-12h sensor is less than 30%, which could be ascribed to the surface-adsorbed H_2O molecules occupying NO_2 sensing sites, which will decrease the adsorbed amount of NO_2 gas molecules [31]. The relatively small attenuation of the sensing response under a high concentration of H_2O molecules in the environment proves that the hierarchical Bi_2S_3 nanostructures have good anti-humidity performance, which could be associated with the improved adsorption of NO_2 molecules with the incorporation of H_2O molecules in Bi_2S_3 [26]. Combined RT resistance variation with sensitivity deviation, the hierarchical Bi_2S_3 sensor could be used to obtain NO_2 concentration information under different humidity atmospheres using the humidity compensation method.

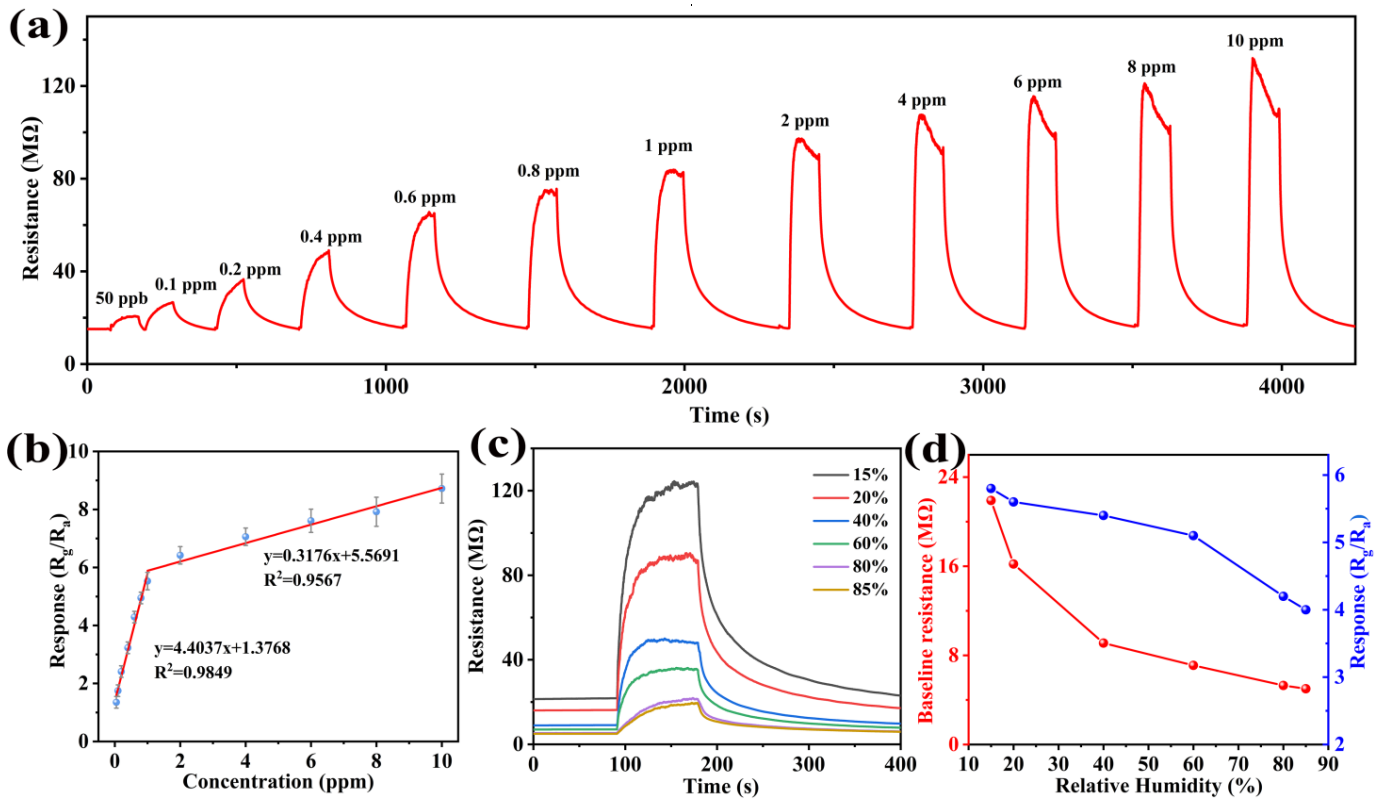

Figure 4. The RT NO_2 sensing properties test of the BS-12h sensor: (**a**) Dynamic NO_2 sensing response curves with different concentrations. (**b**) Linear relationship fitting curve. (**c**) Repeatability toward 1 ppm NO_2. (**d**) Selective response toward interfering gases.

The selectivity of the sensor based on the BS-12h sample was investigated to further recognize the specific interaction between hierarchical Bi_2S_3 nanostructures and NO_2 molecules. Figure 5a shows the sensing response of several kinds of interfered gases, including the main hazardous gases (H_2S, CO, SO_2, and NH_3) and green energy gas (H_2) existing in the atmosphere. The sensitivity of the BS-12h sensor at RT to 100 ppm H_2S, CO, SO_2, NH_3, and H_2 gas is 1.64, 1.07, 1.02, 1.07, and 1.07, respectively. Compared with the sensitivity of 5.8 to 1 ppm NO_2, these results confirm the optimal RT NO_2 detection performance of Bi_2S_3 sensing materials. The intrinsic mechanism of the selectivity of pristine Bi_2S_3 to NO_2 has been investigated using first-principle calculations [26]. The calculated adsorption energy between Bi_2S_3 nanomaterials and NO_2 molecules is much larger than that of the other interfered gases, which results in the excellent detection ability of NO_2 gas. Meanwhile, the newly formed O-S chemical bonds between NO_2 molecules and Bi_2S_3 further enhance the selectivity.

Repeatability and long-term stability are also key properties of gas sensors. The five consecutive cyclic response/recovery curves of the BS-12h sensor are shown in Figure 5b. Obviously, the fluctuation of the sensing response resistance of the BS-12h sensor is negligible, indicating the optimal NO_2 sensing repeatability of the hierarchical Bi_2S_3 nanomaterials. The long-term stability of the sensor based on the BS-12h sample was also acquired by measuring the sensing behaviors toward 1 ppm NO_2 at RT after aging for 60 days (Figure 5c). The sensing response values are in the range of (5.6 $\pm$ 0.3) during 60 days of aging, which shows the hierarchical Bi_2S_3 sensors can acquire stable NO_2 concentration data. The insert of Figure 5c shows the dynamic response data of the sensor based on the BS-12h sample to 1 ppm NO_2 at RT after aging for 30 and 60 days. The BS-12h sensor, after different aging times, displays fast response speed and full-recovery sensing properties at RT. In comparison to the dynamic resistance curve of the BS-12h sensor after aging for 60 days (Figure S6),

the response/recovery time and RT resistance value display a negligible deviation. These results demonstrate its superior stability.

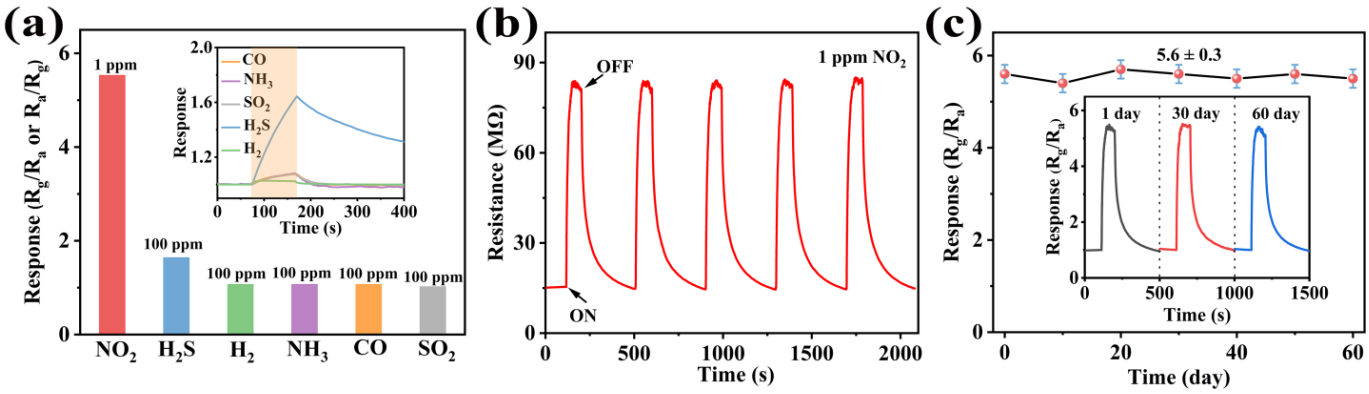

Figure 5. The RT NO_2 sensing properties test of the BS-12h sensor: (**a**) Anti-humidity ability to 1 ppm NO_2 under different relative humidity. (**b**) Baseline resistance and sensitivity to 1 ppm NO_2 under varied humidity environments. (**c**) Long-term stability.

The NO_2 sensing properties of typical metal sulfide-based gas sensors in the literature and our prepared 1D nanorods with self-assembled Bi_2S_3 hierarchical structures are summarized in Table 1. The Bi_2S_3 nanostructures display obviously competitive NO_2 sensing properties, such as high sensitivity, fast response, recovery speed, and low LOD at RT. Combined with the simple prepared means, the synthesized hierarchical Bi_2S_3 nanostructures as NO_2 sensing materials are suitable for practical production.

Table 1. Comparison of NO_2 sensing behaviors of reported metal sulfide nanomaterials and our prepared hierarchical Bi_2S_3 nanostructures.

Materials	NO_2 Conc. (ppm)	Response	τ_{res}/τ_{rec} (s/s)	LOD (ppb)	Reference
WS_2 nanosheets	10	1.4	45/60	2000	[51]
WSe_2 nanosheets	1	1.3	66/1020	100	[52]
SnS_2 nanograins	10	7.0	272/3800	1000	[53]
$SnSe_2$ nanosheets	1	1.6	142/935	100	[54]
MoS_2 nanograins	500	3.5	~180/~480	25,000	[55]
$MoSe_2$ nanosheets	5	1.4	450/600	5000	[56]
NbS_2 nanosheets	5	1.2	~3000/~9000	241	[57]
Bi_2S_3 nanobelts	1	6.9	72/400	500	[21]
CuS/Bi_2S_3 nanosheets	10	3.4	18/388	500	[27]
Au/Bi_2S_3 nanosheets	5	5.6	18/338	250	[28]
Bi_2S_3 hierarchical nanostructures	1	5.8	28/116	50	This study

3.3. Gas Sensing Mechanism

The sensing mechanism of metal sulfide nanomaterials relies on the electron-migration case between the surface of nanostructures and adsorbed target gas molecules [58–60]. The Bi_2S_3 nanomaterials as n-type semiconductors exhibit increased resistance during the electrophilic NO_2 sensing process. In order to confirm the role of O_2 molecules during the NO_2 sensing process of Bi_2S_3 nanostructures, a dynamic gas dilution system was adopted to control the O_2 concentration during the NO_2 sensing test process. The dynamic NO_2 sensing curve with different O_2 concentrations and N_2 as a balance gas is shown in Figure 6. The BS-12h sensor based on hierarchical Bi_2S_3 nanostructures shows an optimum dynamic response/recovery process to 1 ppm NO_2 in different O_2 concentrations. The sensitivity of the BS-12h sensor displays a decline trend, which could be associated with more O_2 molecules trapped on the surface of Bi_2S_3 nanostructures with the increasing O_2

concentration [30]. The RT resistances of the prepared Bi_2S_3 nanostructures under different O_2 concentrations (N_2 as a balance gas) are shown in Figure S7. The resistance value of Bi_2S_3 nanostructures in a 100% N_2 atmosphere is the smallest and exhibits a gradually increasing trend with increasing O_2 concentration. The phenomenon confirms that O_2 molecules can be trapped on the surface of Bi_2S_3 nanostructures and capture electrons from their conduction band to form O_2^-. Upon exposure to NO_2, these NO_2 molecules competitively adsorb on the sensing active sites and trap the electron to form NO_2^-. The little fluctuation in the sensing response of the Bi_2S_3 nanostructures can be associated with the much bigger adsorption energy of NO_2 molecules than that of O_2 molecules [26]. The result confirms that ambient O_2 molecules are not directly involved in NO_2 sensitive processes in Bi_2S_3 nanomaterials. The electron transfer process between the NO_2 molecules and Bi_2S_3 nanostructures could be depicted using the following equation:

$$NO_2\ (gas) + e^- \rightarrow NO_2^-\ (ads) \quad (1)$$

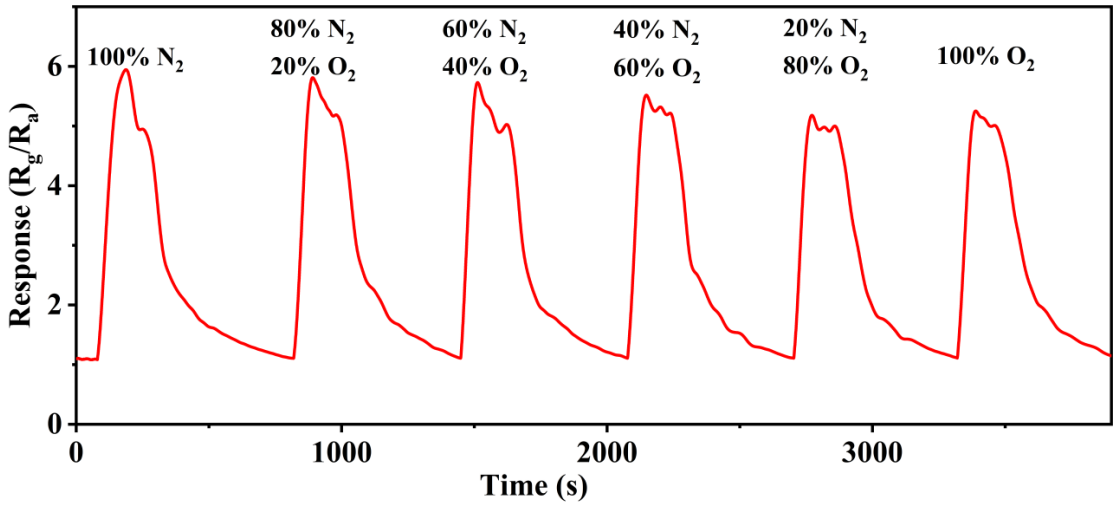

Figure 6. Dynamic RT response/recovery curve of the hierarchical Bi_2S_3 sensor based on the BS-12h sample to 1 ppm NO_2 in 100% N_2, 100% O_2, and different O_2 concentration with N_2 as a balance gas.

The schematic diagram of the NO_2 sensing mechanism of hierarchical Bi_2S_3 nanostructures is shown in Figure 7. The NO_2 molecules adsorb on the surface of the Bi_2S_3 nanostructure and trap electrons, which leads to decreased electron density in Bi_2S_3 and the formation of an electron depletion layer. The formed electron depletion layer on the surface of the sensing materials will cause the resistance of the Bi_2S_3 nanomaterials to increase. When the Bi_2S_3 nanostructure is re-exposed to air, NO_2 molecules gradually finish the desorption process and release the electron to the surface of Bi_2S_3, which results in the resistance value of the sensor recovering up to its baseline resistance.

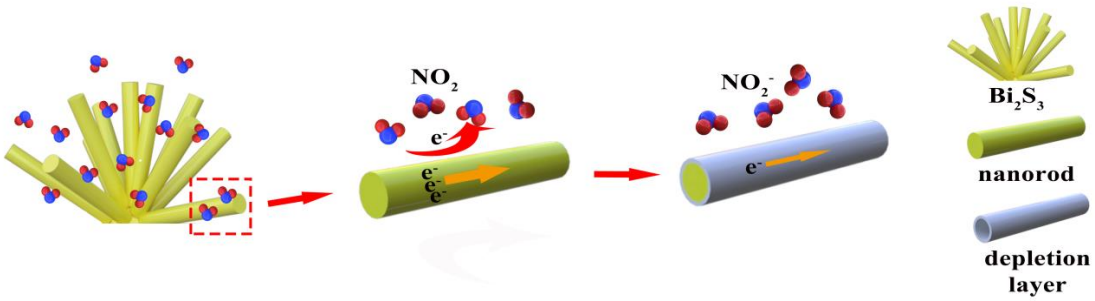

Figure 7. Schematic illustration of the NO_2 sensing mechanism of the 1D nanorod-assembled Bi_2S_3 nanostructures.

The enhanced RT NO_2 sensing properties of as-prepared hierarchical Bi_2S_3 nanostructures assembled from 1D nanorods can be illustrated by the following factors. Firstly, the 1D nanorods self-assembled Bi_2S_3 nanostructure can adequately prevent the 1D nanorods from restacking together, which will markedly increase the exposure-sensing active surface of Bi_2S_3 materials for NO_2 adsorption. The N_2 adsorption/desorption cycles of as-prepared hierarchical Bi_2S_3 nanostructures (BS-8h, BS-12h, and BS-24h samples) were used to calculate the BET surface areas (Figure S8). The specific surface area of the above three samples is 3.6, 4.2, and 4.0 $m^2\ g^{-1}$, respectively. The BS-12h sample shows a much larger active surface than that of other samples. According to the process of growth of the hierarchical Bi_2S_3 nanostructures, the BS-12h sample displays more 1D nanorod-assembled Bi_2S_3 hierarchical nanostructures than the BS-8h sample (Figure S4), which leads to much larger specific surface areas than that of the BS-8h sample. With increasing the reaction time for 24 h, the nanorods of assembled hierarchical Bi_2S_3 structures become short and thick due to their continuous growth, which decreases the exposed active surface of the as-prepared BS-24h sample. The BS-12h sensor shows superior RT NO_2 sensing properties than that of the other sample, in accordance with the specific surface area test value. The large specific surface areas of the BS-12h sensor will provide a mound of NO_2 sensing active sites, which enhance the NO_2 sensing response due to massive NO_2 molecules adsorbing on the surface of hierarchical Bi_2S_3 nanostructures and accelerating the electron transfer from the surface of Bi_2S_3 materials to NO_2 molecules. In addition, the 1D nanorod-assembled Bi_2S_3 as NO_2 sensing materials exhibit fast response and recovery speed and full-recovery properties, which could be associated with a special hierarchical nanostructure and intrinsic physicochemical characteristics. As the mechanism diagram shows in Figure 7, these adjacent 1D nanorods form a mass of open voids, which, as inner flow passages, will dramatically accelerate the diffusion and adsorption/desorption processes between NO_2 molecules and hierarchical Bi_2S_3 nanostructures. When NO_2 molecules adsorb on the 1D nanorods assembled in Bi_2S_3 hierarchically, the NO_2 molecules rapidly diffuse inward through the inner spread path. On the contrary, upon re-exposure to air, the adsorbed NO_2 molecules rapidly and fully desorb from the surface of hierarchical Bi_2S_3 nanostructures and diffuse into the air. Therefore, the sensor based on the 1D nanorods assembled in Bi_2S_3 hierarchical structures shows short response/recovery times and full recovery performance. Additionally, the Bi_2S_3 materials have high carrier mobility and a narrow bandgap [17–22]. These superb physical properties endow Bi_2S_3 with fast electron transfer speed, which will further shorten the response/recovery time. Above all, the special hierarchical nanostructures and unique intrinsic properties of Bi_2S_3 are advantageous in obtaining high sensitivity and a short response/recovery time at RT.

4. Conclusions

In conclusion, 1D nanorods with a self-assembled Bi_2S_3 hierarchical nanostructure were successfully prepared via a simple hydrothermal process and showed improved RT NO_2 sensing properties. The hierarchical Bi_2S_3-based gas sensor showed a high sensitivity (R_g/R_a = 5.8 at 1 ppm), a low LOD (50 ppb), optimum selectivity, and anti-humidity. The outstanding RT sensing properties were associated with the special hierarchical nanostructures and unique intrinsic properties of Bi_2S_3 materials, which accelerate diffusion, adsorption/desorption, and electron transfer processes between NO_2 molecules and hierarchical Bi_2S_3 nanostructures. Additionally, hierarchical Bi_2S_3 exhibited almost the same sensing response in the absence of O_2 gas. The phenomenon confirms that the sensing mechanism of Bi_2S_3 is different from the chemisorption oxygen model. This study focuses on the fundamental sensing mechanism of the hierarchical Bi_2S_3 and provides a kind of novel nanostructure material for low-concentration NO_2 detection at RT.

Supplementary Materials: The following supporting information can be downloaded at https://www.mdpi.com/article/10.3390/chemosensors12010008/s1, Figure S1: Schematic diagram of the interdigital electrodes, sensors based on different sensing materials, and fixture of sensors; Figure S2: Schematic diagram of the gas sensor dynamic analysis system; Figure S3: The elemental mapping of the BS-12h sample; Figure S4: SEM images of as-prepared samples with different reaction times; Figure S5: RT dynamic response/recovery curves of BS-8h, BS-12h, and BS-24h sensors toward 1 ppm NO_2; Figure S6: The dynamic resistance curve of the BS-12h sensor after aging 60 days toward 1.0 ppm NO_2; Figure S7: The RT resistance of the BS-12h sensor with different O_2 concentration atmosphere; and Figure S8: Nitrogen adsorption/desorption isotherms of as-prepared samples with different reaction times.

Author Contributions: Conceptualization, methodology, validation, formal analysis, investigation, data curation, and writing—original draft, Y.Y.; methodology, investigation, formal analysis, and data curation, C.L.; methodology, writing—review and editing, supervision, and funding acquisition, Y.W.; writing—review and editing, supervision, project administration, and funding acquisition, J.H. All authors have read and agreed to the published version of the manuscript.

Funding: This work was financially supported by the National Natural Science Foundation of China (No. 52272147 and 52272272), the Heilongjiang Touyan Team (HITTY-20190034), and the Fundamental Research Funds for the Central Universities (No. 2022FRFK02015).

Institutional Review Board Statement: Not applicable.

Informed Consent Statement: Not applicable.

Data Availability Statement: Data are contained within the article and Supplementary Materials.

Conflicts of Interest: The authors declare no conflicts of interest.

References

1. Ou, J.Z.; Yao, C.K.; Rotbart, A.; Muir, J.G.; Gibson, P.R.; Kalantar-zadeh, K. Human intestinal gas measurement systems: In vitro fermentation and gas capsules. *Trends Biotechnol.* **2015**, *33*, 208–213. [CrossRef] [PubMed]
2. Wong, G.W.K.; Lai, C.K.W. Outdoor air pollution and asthma. *Curr. Opin. Pulm. Med.* **2004**, *10*, 62–66. [CrossRef] [PubMed]
3. Vassilyadi, M.; Michel, R. Effect of methylprednisolone on nitrogen dioxide (NO_2)-induced pulmonary edema in guinea pigs. *Toxicol. Appl. Pharmacol.* **1989**, *97*, 256–266. [CrossRef] [PubMed]
4. Long, H.; Harley-Trochimczyk, A.; Pham, T.; Tang, Z.; Shi, T.; Zettl, A.; Carraro, C.; Worsley, M.A.; Maboudian, R. High surface area MoS_2/graphene hybrid aerogel for ultrasensitive NO_2 detection. *Adv. Funct. Mater.* **2016**, *26*, 5158–5165. [CrossRef]
5. Liu, B.; Chen, L.; Liu, G.; Abbas, A.N.; Fathi, M.; Zhou, C. High-performance chemical sensing using schottky-contacted chemical vapor deposition grown monolayer MoS_2 transistors. *ACS Nano* **2014**, *8*, 5304–5314. [CrossRef] [PubMed]
6. Kawamoto, T.; Matsuno, K.; Arashidani, K.; Yoshikawa, M.; Kodama, Y. Personal exposure to nitrogen dioxide from indoor heaters and cooking stoves. *Arch. Environ. Contam. Toxicol.* **1993**, *25*, 534–538. [CrossRef]
7. Ikram, M.; Liu, L.; Lv, H.; Liu, Y.; Ur Rehman, A.; Kan, K.; Zhang, W.; He, L.; Wang, Y.; Wang, R.; et al. Intercalation of Bi_2O_3/Bi_2S_3 nanoparticles into highly expanded MoS_2 nanosheets for greatly enhanced gas sensing performance at room temperature. *J. Hazard. Mater.* **2019**, *363*, 335–345. [CrossRef] [PubMed]
8. Scott Downen, R.; Dong, Q.; Chorvinsky, E.; Li, B.; Tran, N.; Jackson, J.H.; Pillai, D.K.; Zaghloul, M.; Li, Z. Personal NO_2 sensor demonstrates feasibility of in-home exposure measurements for pediatric asthma research and management. *J. Expo. Sci. Environ. Epidemiol.* **2022**, *32*, 312–319. [CrossRef]
9. Du, Y.; Yu, D.-G.; Yi, T. Electrospun nanofibers as chemosensors for detecting environmental pollutants: A review. *Chemosensors* **2023**, *11*, 208. [CrossRef]
10. Wu, J.; Wu, Z.; Ding, H.; Wei, Y.; Huang, W.; Yang, X.; Li, Z.; Qiu, L.; Wang, X. Flexible, 3D SnS_2/reduced graphene oxide heterostructured NO_2 sensor. *Sens. Actuators B* **2020**, *305*, 127445. [CrossRef]
11. Huang, Y.; Jiao, W.; Chu, Z.; Ding, G.; Yan, M.; Zhong, X.; Wang, R. Ultrasensitive room temperature ppb-level NO_2 gas sensors based on SnS_2/rGO nanohybrids with p–n transition and optoelectronic visible light enhancement performance. *J. Mater. Chem. C* **2019**, *7*, 8616–8625. [CrossRef]
12. Shafiei, M.; Bradford, J.; Khan, H.; Piloto, C.; Wlodarski, W.; Li, Y.; Motta, N. Low-operating temperature NO_2 gas sensors based on hybrid two-dimensional SnS_2-reduced graphene oxide. *Appl. Surf. Sci.* **2018**, *462*, 330–336. [CrossRef]
13. Li, G.; Zhu, X.; Liu, J.; Li, S.; Liu, X. Metal oxide semiconductor gas sensors for lung cancer diagnosis. *Chemosensors* **2023**, *11*, 251. [CrossRef]
14. Hu, Z.; Zhou, L.; Li, L.; Ying, B.; Zhao, Y.; Wang, P.; Li, H.; Zhang, Y.; Liu, H. Quantum dots-sensitized high electron mobility transistor (HEMT) for sensitive NO_2 detection. *Chemosensors* **2023**, *11*, 252. [CrossRef]

15. Tang, T.; Li, Z.; Cheng, Y.; Xu, K.; Xie, H.; Wang, X.; Hu, X.; Yu, H.; Zhang, B.; Tao, X.; et al. Single-step growth of p-type 1D Se/2D $GeSe_xO_y$ heterostructures for optoelectronic NO_2 gas sensing at room temperature. *J. Mater. Chem. A* **2023**, *11*, 6361–6374. [CrossRef]
16. Tang, T.; Li, Z.; Cheng, Y.; Xie, H.; Wang, X.; Chen, Y.; Cheng, L.; Liang, Y.; Hu, X.; Hung, C.; et al. In-situ mechanochemically tailorable 2D gallium oxyselenide for enhanced optoelectronic NO_2 gas sensing at room temperature. *J. Hazard. Mater.* **2023**, *451*, 131184. [CrossRef]
17. Ni, J.; Zhao, Y.; Liu, T.; Zheng, H.; Gao, L.; Yan, C.; Li, L. Strongly coupled Bi_2S_3@CNT hybrids for robust lithium storage. *Adv. Energy Mater.* **2014**, *4*, 1400798. [CrossRef]
18. Dong, Y.; Hu, M.; Zhang, Z.; Zapien, J.A.; Wang, X.; Lee, J.-M. Hierarchical self-assembled Bi_2S_3 hollow nanotubes coated with sulfur-doped amorphous carbon as advanced anode materials for lithium ion batteries. *Nanoscale* **2018**, *10*, 13343–13350. [CrossRef]
19. Bernechea, M.; Cao, Y.; Konstantatos, G. Size and bandgap tunability in Bi_2S_3 colloidal nanocrystals and its effect in solution processed solar cells. *J. Mater. Chem. A* **2015**, *3*, 20642–20648. [CrossRef]
20. Guo, Y.; Ao, Y.; Wang, P.; Wang, C. Mediator-free direct dual-z-scheme $Bi_2S_3/BiOV_4/MgIn_2S_4$ composite photocatalysts with enhanced visible-light-driven performance towards carbamazepine degradation. *Appl. Catal. B* **2019**, *254*, 479–490. [CrossRef]
21. Kan, H.; Li, M.; Song, Z.; Liu, S.; Zhang, B.; Liu, J.; Li, M.-Y.; Zhang, G.; Jiang, S.; Liu, H. Highly sensitive response of solution-processed bismuth sulfide nanobelts for room-temperature nitrogen dioxide detection. *J. Colloid Interface Sci.* **2017**, *506*, 102–110. [CrossRef] [PubMed]
22. Rath, A.K.; Bernechea, M.; Martinez, L.; Konstantatos, G. Solution-processed heterojunction solar cells based on p-type PbS quantum dots and n-type Bi_2S_3 nanocrystals. *Adv. Mater.* **2011**, *23*, 3712–3717. [CrossRef] [PubMed]
23. Yao, K.; Gong, W.W.; Hu, Y.F.; Liang, X.L.; Chen, Q.; Peng, L.-M. Individual Bi_2S_3 nanowire-based room-temperature H_2 sensor. *J. Phys. Chem. C* **2008**, *112*, 8721–8724. [CrossRef]
24. Fu, T.-X. Gas sensor based on three dimensional Bi_2S_3 nanowires network for ammonia detection at room temperature. *Mater. Res. Bull.* **2018**, *99*, 460–465. [CrossRef]
25. Rosolina, S.M.; Carpenter, T.S.; Xue, Z.L. Bismuth-based, disposable sensor for the detection of hydrogen sulfide gas. *Anal. Chem.* **2016**, *88*, 1553–1558. [CrossRef] [PubMed]
26. Feng, Q.; Xie, X.; Zhang, M.; Liao, N. First-principles investigation of Bi_2S_3 as sensitive and selective NO_2 sensor upon humidity exposure. *J. Mater. Sci.* **2023**, *58*, 2198–2208. [CrossRef]
27. Chen, X.; Shi, J.; Wang, T.; Zheng, S.; Lv, W.; Chen, X.; Yang, J.; Zeng, M.; Hu, N.; Su, Y.; et al. High-performance wearable sensor inspired by the neuron conduction mechanism through gold-induced sulfur vacancies. *ACS Sens.* **2022**, *7*, 816–826. [CrossRef]
28. Chen, X.; Wang, T.; Shi, J.; Lv, W.; Han, Y.; Zeng, M.; Yang, J.; Hu, N.; Su, Y.; Wei, H.; et al. A novel artificial neuron-like gas sensor constructed from CuS quantum dots/Bi_2S_3 nanosheets. *Nano-Micro Lett.* **2021**, *14*, 8. [CrossRef]
29. Luo, J.; Feng, X.; Kan, H.; Li, H.; Fu, C. One-dimensional Bi_2S_3 nanobelts-based surface acoustic wave sensor for NO_2 detection at room temperature. *IEEE Sens. J.* **2021**, *21*, 1404–1408. [CrossRef]
30. Liu, D.; Tang, Z.; Zhang, Z. Nanoplates-assembled SnS_2 nanoflowers for ultrasensitive ppb-level NO_2 detection. *Sens. Actuators B* **2018**, *273*, 473–479. [CrossRef]
31. Wang, T.; Wang, Y.; Zheng, S.; Sun, Q.; Wu, R.; Hao, J. Design of hierarchical $SnSe_2$ for efficient detection of trace NO_2 at room temperature. *CrystEngComm* **2021**, *23*, 6045–6052. [CrossRef]
32. Zhang, Y.; Zeng, W.; Li, Y. Hydrothermal synthesis and controlled growth of hierarchical 3D flower-like MoS_2 nanospheres assisted with CTAB and their NO_2 gas sensing properties. *Appl. Surf. Sci.* **2018**, *455*, 276–282. [CrossRef]
33. Fang, L.; Qiu, Y.; Zhai, T.; Wang, F.; Lan, M.; Huang, K.; Jing, Q. Flower-like nanoarchitecture assembled from Bi_2S_3 nanorod/MoS_2 nanosheet heterostructures for high-performance supercapacitor electrodes. *Colloids Surf. A* **2017**, *535*, 41–48. [CrossRef]
34. Lu, J.; Han, Q.; Yang, X.; Lu, L.; Wang, X. Microwave-assisted synthesis and characterization of 3D flower-like Bi_2S_3 superstructures. *Mater. Lett.* **2007**, *61*, 2883–2886. [CrossRef]
35. Tang, J.; Alivisatos, A.P. Crystal splitting in the growth of Bi_2S_3. *Nano Lett.* **2006**, *6*, 2701–2706. [CrossRef] [PubMed]
36. Shen, G.; Chen, D.; Tang, K.; Li, F.; Qian, Y. Large-scale synthesis of uniform urchin-like patterns of Bi_2S_3 nanorods through a rapid polyol process. *Chem. Phys. Lett.* **2003**, *370*, 334–337. [CrossRef]
37. Kumari, P.; Awasthi, K.; Agarwal, S.; Ichikawa, T.; Kumar, M.; Jain, A. Flower-like Bi_2S_3 nanostructures as highly efficient anodes for all-solid-state lithium-ion batteries. *RSC Adv.* **2019**, *9*, 29549–29555. [CrossRef]
38. Li, H.; Yang, J.; Zhang, J.; Zhou, M. Facile synthesis of hierarchical Bi_2S_3 nanostructures for photodetector and gas sensor. *RSC Adv.* **2012**, *2*, 6258. [CrossRef]
39. Zheng, S.; Yin, D.; Zhang, S.; Wang, Y.; Li, J.; Wang, Z.; Yuan, Y.; Tsai, H.-S.; Hao, J. Tailoring selenium vacancies in $MoSe_2$ through oxygen passivation for room-temperature NO_2 sensing enhancement. *J. Mater. Chem. A* **2023**, *11*, 18755. [CrossRef]
40. Miller, D.R.; Akbar, S.A.; Morris, P.A. Nanoscale metal oxide-based heterojunctions for gas sensing: A review. *Sens. Actuators B* **2014**, *204*, 250–272. [CrossRef]
41. Hao, J.; Zhang, D.; Sun, Q.; Zheng, S.; Sun, J.; Wang, Y. Hierarchical SnS_2/SnO_2 nanoheterojunctions with increased active-sites and charge transfer for ultrasensitive NO_2 detection. *Nanoscale* **2018**, *10*, 7210–7217. [CrossRef] [PubMed]
42. Yang, X.; Tian, S.; Li, R.; Wang, W.; Zhou, S. Use of single-crystalline Bi_2S_3 nanowires as room temperature ethanol sensor synthesized by hydrothermal approach. *Sens. Actuators B* **2017**, *241*, 210–216. [CrossRef]

43. Yu, Y.; Jin, C.H.; Wang, R.H.; Chen, Q.; Peng, L.M. High-quality ultralong Bi_2S_3 nanowires: structure, growth, and properties. *J. Phys. Chem. B* **2005**, *109*, 18772–18776. [CrossRef] [PubMed]
44. Cheng, Y.; Chang, Y.; Feng, Y.; Jian, H.; Tang, Z.; Zhang, H. Deep-level defect enhanced photothermal performance of bismuth sulfide–gold heterojunction nanorods for photothermal therapy of cancer guided by computed tomography imaging. *Angew. Chem. Int. Ed.* **2018**, *57*, 246–251. [CrossRef] [PubMed]
45. Grigas, J.; Talik, E.; Lazauskas, V. X-ray photoelectron spectra and electronic structure of Bi_2S_3 crystals. *Phys. Status Solidi* **2002**, *232*, 220–230. [CrossRef]
46. Sun, Q.; Wang, J.; Hao, J.; Zheng, S.; Wan, P.; Wang, T.; Fang, H.; Wang, Y. SnS_2/SnS p-n heterojunctions with an accumulation layer for ultrasensitive room-temperature NO_2 detection. *Nanoscale* **2019**, *11*, 13741–13749. [CrossRef] [PubMed]
47. Cui, S.; Pu, H.; Wells, S.A.; Wen, Z.; Mao, S.; Chang, J.; Hersam, M.C.; Chen, J. Ultrahigh sensitivity and layer-dependent sensing performance of phosphorene-based gas sensors. *Nat. Commun.* **2015**, *6*, 8632. [CrossRef] [PubMed]
48. Li, Y.; Song, Z.; Li, Y.; Chen, S.; Li, S.; Li, Y.; Wang, H.; Wang, Z. Hierarchical hollow MoS_2 microspheres as materials for conductometric NO_2 gas sensors. *Sens. Actuators B* **2019**, *282*, 259–267. [CrossRef]
49. Han, Y.; Liu, Y.; Su, C.; Wang, S.; Li, H.; Zeng, M.; Hu, N.; Su, Y.; Zhou, Z.; Wei, H.; et al. Interface engineered WS_2/ZnS heterostructures for sensitive and reversible NO_2 room temperature sensing. *Sens. Actuators B* **2019**, *296*, 126666. [CrossRef]
50. Guo, R.; Han, Y.; Su, C.; Chen, X.; Zeng, M.; Hu, N.; Su, Y.; Zhou, Z.; Wei, H.; Yang, Z. Ultrasensitive room temperature NO_2 sensors based on liquid phase exfoliated WSe_2 nanosheets. *Sens. Actuators B* **2019**, *300*, 127013. [CrossRef]
51. Simon Patrick, D.; Bharathi, P.; Krishna Mohan, M.; Muthamizchelvan, C.; Harish, S.; Navaneethan, M. Liquid phase exfoliated WS_2 nanosheet-based gas sensor for room temperature NO_2 detection. *J. Mater. Sci. Mater. Electron.* **2022**, *33*, 9235–9245. [CrossRef]
52. Duan, Y.; Feng, S.; Zhang, K.; Qiu, J.; Zhang, S. Vertical few-layer WSe_2 nanosheets for NO_2 sensing. *ACS Appl. Nano Mater.* **2021**, *4*, 12043–12050. [CrossRef]
53. Kwon, K.C.; Suh, J.M.; Lee, T.H.; Choi, K.S.; Hong, K.; Song, Y.G.; Shim, Y.-S.; Shokouhimehr, M.; Kang, C.-Y.; Kim, S.Y.; et al. SnS_2 nanograins on porous SiO_2 nanorods template for highly sensitive NO_2 sensor at room temperature with excellent recovery. *ACS Sens.* **2019**, *4*, 678–686. [CrossRef] [PubMed]
54. Camargo Moreira, Ó.L.; Cheng, W.-Y.; Fuh, H.-R.; Chien, W.-C.; Yan, W.; Fei, H.; Xu, H.; Zhang, D.; Chen, Y.; Zhao, Y.; et al. High selectivity gas sensing and charge transfer of $SnSe_2$. *ACS Sens.* **2019**, *4*, 2546–2552. [CrossRef] [PubMed]
55. Zhao, Y.; Song, J.-G.; Ryu, G.H.; Ko, K.Y.; Woo, W.J.; Kim, Y.; Kim, D.; Lim, J.H.; Lee, S.; Lee, Z.; et al. Low-temperature synthesis of 2D MoS_2 on a plastic substrate for a flexible gas sensor. *Nanoscale* **2018**, *10*, 9338–9345. [CrossRef] [PubMed]
56. Zhang, S.; Nguyen, T.H.; Zhang, W.; Park, Y.; Yang, W. Correlation between lateral size and gas sensing performance of $MoSe_2$ nanosheets. *Appl. Phys. Lett.* **2017**, *111*, 161603. [CrossRef]
57. Kim, Y.; Kwon, K.C.; Kang, S.; Kim, C.; Kim, T.H.; Hong, S.-P.; Park, S.Y.; Suh, J.M.; Choi, M.-J.; Han, S.; et al. Two-dimensional NbS_2 gas sensors for selective and reversible NO_2 detection at room temperature. *ACS Sens.* **2019**, *4*, 2395–2402. [CrossRef]
58. Bag, A.; Lee, N.-E. Gas sensing with heterostructures based on two-dimensional nanostructured materials: A review. *J. Mater. Chem. C* **2019**, *7*, 13367–13383. [CrossRef]
59. Zappa, D.; Galstyan, V.; Kaur, N.; Munasinghe Arachchige, H.M.M.; Sisman, O.; Comini, E. "Metal oxide-based heterostructures for gas sensors"—A review. *Anal. Chim. Acta* **2018**, *1039*, 1–23. [CrossRef]
60. Lee, E.; Yoon, Y.S.; Kim, D.J. Two-dimensional transition metal dichalcogenides and metal oxide hybrids for gas sensing. *ACS Sens.* **2018**, *3*, 2045–2060. [CrossRef]